

## Deformed wavelength-scale microdisk lasers with quantum dot emitters

---

J-B. SHIM A. EBERSPÄCHER and J. WIERSIG, Universität Magdeburg, Germany, J. UNTERHINNINGHOFEN, OEC AG, Germany, Q. H. SONG, Harbin Institute for Technology, China, L. GE, Princeton University, USA, H. CAO and A. D. STONE, Yale University, USA

**Abstract:** A recent development in the fabrication of quantum dot based microdisk lasers is the ability to reduce their dimensions to approximately the emission wavelength. In this chapter we show that deforming the cross-sectional shape of such disk lasers can lead to highly directional light output from high-quality modes. The directional emission results from weak coupling of isotropic high-quality modes to anisotropic low-quality modes, combined with chiral symmetry breaking of clockwise and counterclockwise propagating waves. The fact that the quality factor stays high is explained by the existence of partial barriers in the phase space of ray dynamics. These two mechanisms make it possible to control the output properties of wavelength-scale lasers.

**Key words:** deformed microdisks, quantum dot microcavity lasers, quantum chaos, ray-wave correspondence.

### 7.1 Introduction

Optical microcavities have been extensively studied to probe cavity quantum electrodynamic effects in the solid state and to provide useful on-chip integrated optical devices such as add-drop filters, modulators and laser light sources. However, for over a decade, another focus of microcavity, and specifically microlaser, research has been on novel effects relating to classical/ray and quantum/wave chaos, which affect the emission patterns and quality ( $Q$ ) factors of such lasers. The key idea, introduced by Nöckel, Stone and Chang in 1994 (Nöckel *et al.*, 1994), and extended and tested by Nöckel and Stone in 1997 (Nöckel, 1997), was to regard microdisk cavities as ‘leaky’ billiards, for which the emission patterns and lifetimes could be calculated, at least in useful limits, via a simple ‘ray escape’ model.

A billiard is a planar region with perfect specularly reflecting walls, confining the motion of a point particle; such systems have been studied extensively in the non-linear dynamics community as a tractable model for understanding

chaos and the transition to chaos in conservative Hamiltonian dynamics. In the formal analogy to optics, the point particles become light rays, which are specularly reflected from the walls of the microcavity, but unlike standard billiards, can refractively (or evanescently) escape at each bounce, in addition to the probability of specular reflection. Of particular interest are optical cavities that are obtained by smoothly deforming a circle (or cylinder). In this case the ray motion undergoes the well-known Kolmogorov–Arnold–Moser transition to chaos, in which the system passes through the regime of ‘mixed phase space’ or ‘soft chaos’, where the phase space has a combination of chaotic and regular regions. As the chaotic regions increase, large scale ‘chaotic diffusion’ in the phase space becomes possible, both allowing enhanced ray escape and breaking the emission isotropy of the modes of circular micro-disk lasers, which had been well-studied prior to this work. Surprisingly, the initial work on this problem found that relatively highly directional emission became possible due to this chaotic ray diffusion, raising the possibility of using this approach to enhance the coupling of laser light out of the cavity in preferred directions, without adding additional guiding elements and without reducing the cavity  $Q$  to unacceptable levels. Such smoothly deformed microdisk and microcylinder cavities are termed ‘asymmetric resonant cavities’ (ARCs) (Nöckel, 1997), and there is by now a substantial body of both experimental and theoretical work studying such ARC lasers.

The initial theory consisted of a sampled ray model (henceforth ‘the ray model’), along with an adiabatic approximation for phase space flow (Nöckel, 1997), which assumes that the curvature of the cavity boundary varies slowly on the length scale set by the distance between successive reflections of a ray at the boundary. In this ray model, a set of initial rays were distributed uniformly in the relevant region of phase space and then propagated forward in time using the ‘billiard map’ for a specific cavity shape, which was modified to allow refraction and reflection, according to the laws of Fresnel and Snell, until most of the rays had escaped. The mean escape time was measured, yielding an average  $Q$  of the resonator, and a histogram of escaping ray density in the far-field provided a ‘classical’ prediction for the emission pattern of ARC lasers, which agreed remarkably well with full electromagnetic solutions for the high- $Q$  resonances (Nöckel, 1997). The high emission directions were described qualitatively in the frame of the adiabatic approximation initially, but turned out to be much more robust than expected from that model, which should fail when the system is too chaotic. Schwefel *et al.* (2004) identified a mechanism for robust and universal directional emission from ARC lasers, based on the ‘unstable manifolds’ of short trapped periodic orbits (ray trajectories), which define the paths in phase space for rapid and hence dominant escape. This approach was able to predict and explain the high emission directions from ARC lasers just from the studying of a few short periodic orbits (Schwefel *et al.*, 2004), and

also clarified why ARC shapes with highly chaotic dynamics might nonetheless exhibit very directional emission patterns. It should be noted the utility of the ray model is highest for relatively large microcavities, for which the deformation cannot be treated perturbatively, and for which numerical solutions are difficult, although feasible. In these cases, in which, due to non-separability of the wave equation, there are no simple solutions in terms of special functions, nor any conserved quantum numbers, such as angular momentum, the ray model provides a critical understanding of the numerical solutions as well.

However, the ray model, augmented by the unstable manifold picture, is still a classical model, which neglects interference effects and other non-classical effects such as photon tunneling (evanescent leakage). This was pointed out in the initial work on ARCs (Nöckel, 1997), and becomes a more salient shortcoming when one begins to study ARCs that are approaching the wavelength scale, as seen in the current work. In fact restoring wave effects, while still maintaining the useful understanding provided by classical dynamics, is precisely the problem of quantum chaos (Stöckmann, 2000) (when using the Schrödinger equation), or ‘wave chaos’ when applied to classical wave equations, such as those of electromagnetism. In particular, in the study of quantum/wave chaos it is well-known that classical structures that do not prevent phase space flow, nonetheless reduce the flow of waves, crudely speaking, because the waves find it difficult to penetrate subwavelength regions. This is a major effect in the systems we investigate here.

Although there were extensive experimental studies of ARC lasers in the years after they were proposed, all of the initial studies were focused on cavities that retained two discrete reflection symmetry planes, and were found to emit multiple output beams. For applications it is of course desirable to design an ARC that emits a unidirectional beam, like a conventional laser. However, there appeared to be a basic problem with obtaining such a cavity. ARCs are dielectric cavities, which exploit the high reflectivity of a dielectric boundary near the total internal reflection condition to achieve relatively high- $Q$  resonances. Thus the relevant ray trajectories must have a reasonably high angle of incidence. If such trajectories are associated with periodic orbits, then the opposite sense of rotation, which should also contribute to the laser emission, would produce an output beam in a second, distinct direction.

Nonetheless, a few years ago, Wiersig and Hentschel showed that an ARC microcavity exists that leads to high- $Q$  resonances with unidirectional emission, both within the ray model and in agreement with electromagnetic simulations (Wiersig and Hentschel, 2008). The cavity boundary is defined by the limaçon of Pascal, which represents a dipolar distortion of the circle. Although the intracavity ray dynamics is predominantly chaotic, wave localization on the unstable periodic orbits (this effect is called ‘scarring’;

Heller, 1984) above the critical angle for total internal reflection leads to the formation of high- $Q$  modes. The output directionality is universal for all of these high- $Q$  ‘scarred’ modes because the corresponding escape routes of rays are along the unstable manifolds (Schwefel *et al.*, 2004; Wiersig and Hentschel, 2008). These manifolds are not symmetric under reversal of the sense of rotation, and so can produce unidirectional emission, unlike ray emission directly from unstable periodic orbits.

Several experiments quickly followed, including some by the current authors, and confirmed this prediction with various material systems (Shinohara *et al.*, 2009; Song *et al.*, 2009b; Yan *et al.*, 2009; Yi *et al.*, 2009). In our initial experiments on limaçon ARC lasers, we studied a GaAs microdisk with embedded InAs quantum dots (QDs) as the gain medium with lateral dimensions slightly less than 5  $\mu\text{m}$ . The measured  $Q$ -factor is about 22 000, significantly higher than all the previously reported  $Q$  values of deformed microcavities (Chern *et al.*, 2003; Gao *et al.*, 2007). The high-quality factor and small modal volume result in very low lasing threshold, allowing continuous wave operation. The inhomogeneously broadened gain spectrum of InAs QDs leads to lasing in multiple modes well separated in wavelength. All the lasing modes have single output beam in the same direction, regardless of their wavelengths and intracavity mode structures. The unidirectionality is robust against cavity sidewall roughness and small shape deviation, allowing fabrication by standard photolithography and wet chemical etching.

Although the above-mentioned microcavity laser (Song *et al.*, 2009b) is smaller than the limaçon -shaped microcavities made by other groups (Shinohara *et al.*, 2009; Yan *et al.*, 2009; Yi *et al.*, 2009), its dimensions are still significantly larger than the wavelength of the emitted light. Thus we were motivated to push the cavity size down to wavelength scale, to check if and when the universal directional emission predicted by the ray model would break down. As noted wave corrections to the ray model are expected to appear as the wavelength approaches the cavity size. It is therefore interesting to see if smoothly deformed *wavelength-scale* cavities can still achieve simultaneously unidirectional emission and high  $Q$ -factor, and under what conditions. In recent experiments (Song *et al.*, 2010) we did observe unidirectional emission from wavelength-scale lasers, and we found that it arises from the coupling of relatively high- $Q$  resonances to more directional lower- $Q$  scarred resonances based on specific unstable periodic orbits. In contrast to the prediction of the ray model, the directionality has turned out to be non-universal, with bidirectional emission also seen, in agreement with electromagnetic simulations. These experiments and their interpretation led to generalizations of the ray model that break the chiral symmetry of emission based on periodic orbits, as will be explained below. Thus we find the classical phase space picture, suitably modified, can give insight into the behavior of wavelength-scale ARC lasers.

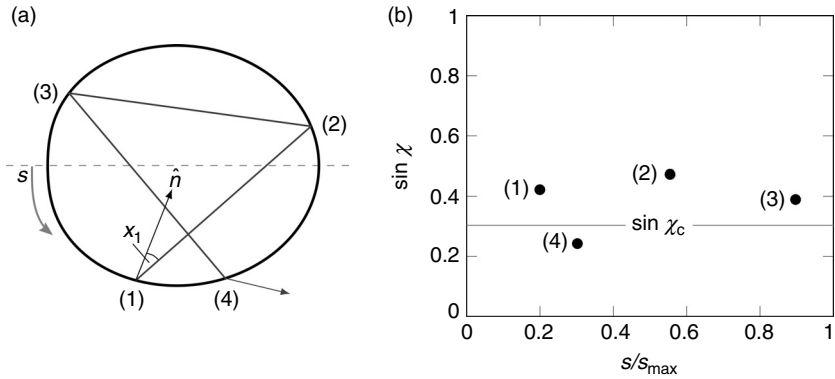
## 7.2 Ray-wave correspondence in microdisk cavities

In the effective-index approximation for (deformed) microdisks Maxwell's equations reduce to a two-dimensional scalar mode equation (Jackson, 1962)

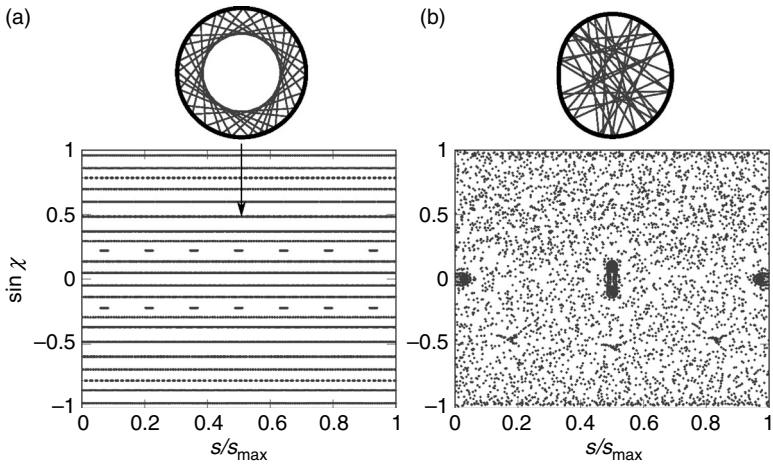
$$-\nabla^2 \psi = n^2(x, y) \frac{\omega^2}{c^2} \psi, \quad [7.1]$$

with piece-wise constant effective index of refraction  $n(x, y)$ , frequency  $\omega = ck$ , wave number  $k$  in vacuum (outside the disk), and the speed of light in vacuum  $c$ . For simplicity we neglect a possible frequency dependence of the refractive index. The mode equation [7.1] is valid for both transverse magnetic (TM) and transverse electric (TE) polarization. For TM polarization the electric field  $\vec{E}(x, y, t) \propto (0, 0, \text{Re}[\psi(x, y)e^{-i\omega t}])$  is perpendicular to the cavity plane. The wave function  $\psi$  and its normal derivative  $\partial_\nu \psi$  are continuous across the boundary of the cavity. For TE polarization,  $\psi$  represents the  $z$ -component of the magnetic field vector  $H_z$ . Here,  $\psi$  and  $n(x, y)^{-2} \partial_\nu \psi$  are continuous across the boundaries (Jackson, 1962). At infinity, outgoing wave conditions are imposed that result in quasibound states (resonant modes) with complex frequencies  $\omega$  in the lower half-plane. The imaginary part determines the lifetime  $\tau = 1/[2\text{Im}\omega]$  and the quality factor  $Q = -\text{Re}\omega/[2\text{Im}\omega]$ .

As discussed in the introduction much understanding about the wave dynamics in microcavities can be gained by studying the ray-wave correspondence. A convenient tool to investigate the ray dynamics is the Poincaré surface of section (SOS) (Lichtenberg and Lieberman, 1992). It is a plot of the intersection points of a set of trajectories with a surface in phase space. This is illustrated in Fig. 7.1. Starting with a given trajectory, its position in terms of the arclength coordinate along the circumference  $s$  and the quantity  $p = \sin \chi$  ( $\chi$  is the angle of incidence) are recorded always directly before or after the particle is reflected at the cavity's boundary. With the total momentum being normalized to unity,  $\sin \chi \in [-1, 1]$  can be interpreted as tangential momentum component with respect to the boundary curve at the position  $s \in [0, s_{\text{max}}]$ . We adopt here the convention that  $\sin \chi > 0$  means counterclockwise (CCW) rotation and  $\sin \chi < 0$  means clockwise (CW) rotation. In the so-called Birkhoff coordinates  $(s, \sin \chi)$  (Birkhoff, 1913) the mapping from bounce to bounce,  $(s_i, \sin \chi_i) \rightarrow (s_{i+1}, \sin \chi_{i+1})$ , is area-preserving (Berry, 1981). The key difference between a billiard (closed cavity, with vanishing wave function  $\psi$  along the boundary) and an optical microcavity is that in the former case the ray stays inside the interior of the domain enclosed by the boundary, and in the latter case the ray can leave the cavity when it enters the leaky region where the condition for total internal reflection is not fulfilled; see position (4) in Fig. 7.1.



7.1 Light ray trajectory in a deformed microdisk in real space (a) and in the Poincaré surface of section (b);  $s$  is the arclength coordinate (normalized to the perimeter  $s_{\max}$ ) and  $\chi$  is the angle of incidence (measured with respect to the normal  $\hat{n}$ ). The critical line  $\sin \chi_c = 1/n$  marks the border of the leaky region where the condition for total internal reflection is not fulfilled.



7.2 (a) Circular billiard: whispering gallery ray trajectory in real space and in the Poincaré surface of section. Typical trajectories in this cavity fill a line of constant  $\sin \chi$ . (b) Chaotic trajectory and Poincaré surface of section for the limaçon billiard defined in Equation [7.2] with  $\varepsilon = 0.43$ .

Figure 7.2a illustrates a ray trajectory in a circular billiard. The corresponding modes are called whispering-gallery (WG) modes named after the whispering gallery at the St. Paul’s Cathedral in London (Rayleigh, 1945). In the case of the integrable circular billiard, the conserved angular

momentum is proportional to  $\sin \chi$ . Hence rays are confined to invariant lines of constant  $\sin \chi$ . This has important consequences for the ray dynamics in a microdisk. Consider a ray that initially fulfills the condition for total internal reflection  $|\sin \chi| > 1/n$ . Since the ray does not leave the invariant line  $\sin \chi = \text{const}$ , it cannot enter the leaky region. Hence, the quality factor in a circular microdisk predicted by ray dynamics is infinitely large. However, the (small) wave correction to this picture is given by evanescent leakage, the optical analogue of quantum tunneling, which leads to finite but very high  $Q$ -factors even in the case of an ideal disk.

The rotational symmetry of a circular microdisk results in a uniform far-field emission pattern, which is a considerable disadvantage for most applications, in particular for microlasers. Breaking the rotational symmetry, for example, by deforming the boundary, leads in almost every case to a cavity with partially or fully chaotic ray dynamics and an improved far-field emission pattern (Nöckel *et al.*, 1996; Nöckel and Stone, 1997; Gmachl *et al.*, 1998; Lebental *et al.*, 2006, 2007; Tanaka *et al.*, 2007). To illustrate the ray dynamics in a deformed microcavity, we consider a specific boundary curve, the limaçon of Pascal that reads in polar coordinates  $(\rho, \phi)$

$$\rho(\phi) = R(1 + \varepsilon \cos \phi). \quad [7.2]$$

The limiting case of vanishing deformation parameter  $\varepsilon$  is the circle with radius  $R$ . For sufficiently large deformation parameter  $\varepsilon$  the dynamics is predominately chaotic; see Fig. 7.2b. Only small ‘islands of regularity’ can be observed in the ‘chaotic sea’. A trajectory starting in the chaotic region diffuses in phase space in a chaotic fashion as indicated by the small dots.

### 7.3 Modified ray-wave correspondence in wavelength-scale cavities

Ray models have been highly successful in predicting the properties, in particular the output directionality, of microcavities; however, as smaller cavities are fabricated, wave effects become more important and the ray model can be expected to break down. In the following we discuss two aspects close to this breakdown: (a) recent attempts to amend the ray dynamics by including first-order wave corrections and (b) localization of waves due to partial barriers.

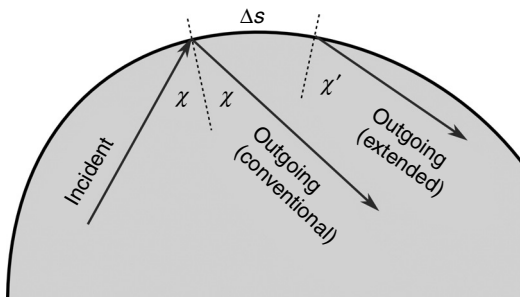
#### 7.3.1 Extended ray dynamics

Two wave corrections that appear naturally in dielectric cavities are the Goos–Hänchen shift (GHS) (Goos and Hänchen, 1947) and the Fresnel

filtering (FF) effect (Tureci and Stone, 2002). Both corrections arise because at finite wavelengths, rays have to be replaced by beams. In the case of the GHS, the different partial waves in such a beam accumulate different phases upon reflection at an interface, which leads to a lateral shift  $\Delta s$  along the interface due to interference. In the case of the FF, partial waves with angles of incidence below the critical angle for total internal reflection  $\chi_c$  are (partially) refracted out of the cavity, giving rise to a shift  $\Delta\chi$  (or  $\Delta p$ , if one considers the dimensionless momenta  $p = \sin \chi$  of the partial waves) between the incident and outgoing angles – that is, a violation of Snell’s law. Figure 7.3 illustrates the two effects. Note that both corrections are absent in billiards.

It is important to mention that if one considers in the ray dynamics not only individual rays but ray *densities* in phase space then the FF is always present. In that sense the FF can be considered as a ray dynamical effect, which is in contrast to the GHS where interference of partial waves is the essential ingredient. Nevertheless, including the FF explicitly in the extended ray dynamics is a powerful tool, as it often allows a description of dynamical properties in terms of a few or even a single ray as we will see later.

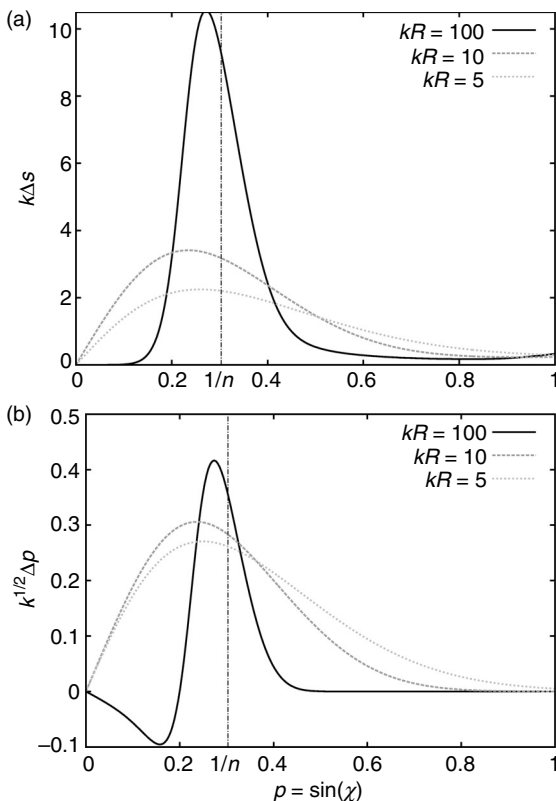
A simple analytical formula for the GHS is due to Artmann (1948); however, it exhibits singularities at the critical angle and at  $\sin \chi = 1$ , both of which are unphysical for beams. Moreover, it is only applicable above the critical angle. For Gaussian beams, there is an analytical result due to Lai *et al.* (1986), which is unfortunately only valid if the beam width  $\sigma$  is much larger than  $1/k$ . In the regime of  $k\sigma \approx 1$ , in which we are interested in, Lai’s formula also shows unphysical singularities (Unterhinninghofen and Wiersig, 2010). For the FF, no analytical results exist so far for the  $p$  dependence of  $\Delta p$ . Hence, it is practical to calculate both the GHS and the FF numerically



7.3 Goos–Hänchen shift  $\Delta s$  and Fresnel filtering  $\Delta p = \sin \chi' - \sin \chi$  as wave corrections to the ray dynamics. A beam is not reflected at the same position on the boundary, but the outgoing beam is shifted by  $\Delta s$ ; the outgoing angle  $\chi'$  is not the same as the incident angle  $\chi$ .

by reflecting Gaussian beams with minimal and equal uncertainties in position and momentum directions on a flat interface (Unterhinninghofen and Wiersig, 2010). Figure 7.4 shows a typical example for the GHS and FF. Measurements of the GHS in the microwave regime have been done by Unterhinninghofen *et al.* (2011).

The extended ray dynamics including GHS and FF has been successfully applied to shed some light on the origin of certain peculiar spectral properties of elliptical microcavities (Unterhinninghofen *et al.*, 2008), of localization properties of mode patterns in spiral microcavities (Altmann *et al.*, 2008) and in other deformed microdisks (Unterhinninghofen and Wiersig, 2010).



7.4 (a) Goos-Hänchen shift and (b) Fresnel filtering calculated for a flat dielectric interface as functions of  $\sin \chi$  for  $n = 3.3$ , TE polarization and different values of the normalized frequency  $(\omega/c)R = kR$ . The Goos-Hänchen shift curves have been scaled with  $k$ , the Fresnel filtering curves with  $\sqrt{k}$  ( $R = 1$ ). The effects are most pronounced near the critical line  $\sin \chi_c = 1/n$ .

### 7.3.2 Whispering-gallery modes trapped by partial barriers

In this section we discuss another interesting aspect that becomes highly relevant for wavelength-scale microdisks, namely the confinement of WG modes by partial barriers. To start with, consider a WG mode in a circular microcavity. It has a definite value of angular momentum due to the rotational symmetry. When the corresponding ray trajectory is plotted on the phase space section using the Birkhoff coordinates, this conserved angular momentum appears as a horizontal line with a specific  $\sin \chi$  value; see Fig. 7.2a. Hence, a given initial condition can reach points only on the same line and there is no trajectory connecting two points on different lines (Fig. 7.5a). Effectively, the trajectory lines in the phase space section play a role of barriers and are accordingly called *dynamical barriers*.

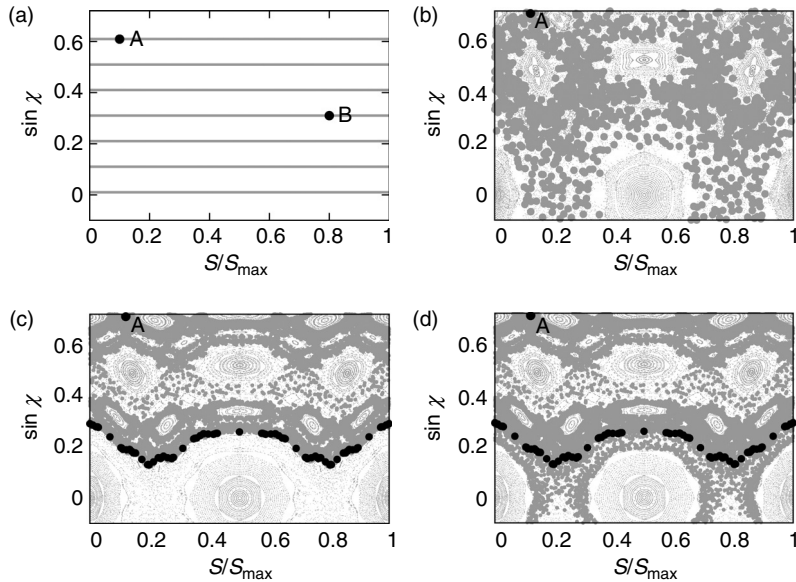
However, if the rotational and the radial degree-of-freedom are non-linearly coupled through deformation of the cavity, the phase space section becomes chaotic. One of the most important features in this chaotic transition is that the dynamical barriers become broken to open new diffusive trajectories. In a unified chaotic area of the phase space, a trajectory that connects infinitesimal areas around two arbitrary points can be found in any case (Fig. 7.5b).

If the deformation or the non-linear coupling is given by a smooth function, the chaotic transition progresses transiently. For example, if the shape of a microcavity is given by the multipolar expansion

$$\rho(\phi) = R \sum_{n=0}^{\infty} (\epsilon_n \cos n\phi + \eta_n \sin n\phi) \quad [7.3]$$

its internal ray dynamics becomes slowly chaotic depending on the deformation parameters  $\epsilon_n$  and  $\eta_n$ . In this process, the dynamical barriers in the phase space do not break abruptly but slowly disappear through an intermediate status, where the dynamical barriers turn into structures similar to Cantor's set, that is, lines with many holes that are fractally distributed. The chaotic diffusion proceeds passing through these holes. Because every dynamical barrier breaks at a different value of the system parameter  $\epsilon_n$  or  $\eta_n$  in Equation [7.3], a slightly broken barrier can still suppress the chaotic diffusion considerably, even if the chaotic area is unified (compare Fig. 7.5c and 7.5d).

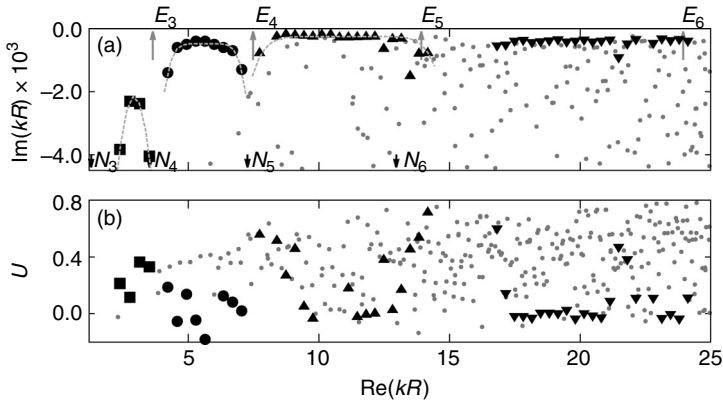
Now, let's imagine a situation where a wave is launched on the phase space and follows the chaotic diffusion. In phase space, the amount of trajectories passing through the broken barrier can be measured by a phase space area. Such an area is given in the unit of action. The whole process is therefore called *action transport*. The comparison of this action with the wave resolution determines how smoothly the wave function follows the



7.5 Phase space portraits of the limaçon shaped microcavity, see Equation [7.2]: (a)  $\varepsilon = 0$  (circle): regular motion. There is no trajectory connecting A and B. (b)  $\varepsilon = 0.28$ : a single trajectory (thick gray dots) starting from A by 1000 iterations. The trajectory diffuses to the lower part of phase space. (c)  $\varepsilon = 0.25$ : single trajectory starting from A by 20 000 iterations. Chaotic diffusion is blocked by a partial barrier (thick black dots). (d)  $\varepsilon = 0.25$ : further progress of the trajectory in (c) by 30 000 iterations. The trajectory penetrates the partial barrier.

chaotic diffusion. If the action of a broken barrier is very tiny in comparison with the resolution limit of the wave, the wave feels this broken barrier as a complete barrier (Shim *et al.*, 2008). From this reasoning, we can deduce that partial barrier's suppressing chaotic diffusion is more conspicuous in wave dynamics and this suppression effect gets stronger with increasing wavelength (or decreasing cavity size).

In this section, the formation of WG modes by partial barriers and their optical properties are discussed in the deep wave regime, that is, in a very tiny microdisk cavity that has a diameter comparable with the vacuum wavelength. In this case, even a periodic orbit with a low period can play a role of a partial barrier to suppress chaotic diffusion. This suppression from the partial barriers induces the unexpected formation of high- $Q$  modes. Using a semiclassical approach the criteria for those high- $Q$  modes can be derived. The discussion starts with a numerically obtained spectrum of a subwavelength-scaled deformed microcavity. Figure 7.6a shows the numerically calculated spectrum of limaçon shaped microcavity, the boundary of which is given by Equation [7.2]. As can be seen by the comparison with Equation



7.6 (a) Calculated spectrum of normalized complex frequencies,  $kR$ , of the limaçon shaped microcavity with  $\epsilon = 0.43$  and  $n = 3$ . Each dot corresponds to a mode. The local maximum of  $Q = -\text{Re}(kR)/2\text{Im}(kR)$  is reached by a convex curve plotted by symbols. The symbols are differed by the geometry of confining partial barrier, square: period 3, circle: period 4, triangle pointing upwards: period 5, triangle pointing downwards: period 6. (b) Corresponding measure of unidirectionality. The opposite tendency to  $Q$ -factors is visible.

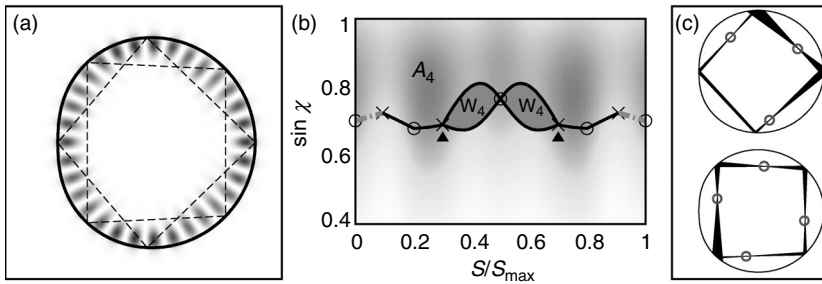
[7.3], the limaçon shape is the lowest term of the multipolar expansion. A microcavity with this shape is known to have a relatively high  $Q$ -factor and unidirectional light emission. These advantageous features of the limaçon shape can be understood by chaotic diffusion (Wiersig and Hentschel, 2008). For the calculation of the spectrum, we set the deformation parameter,  $\epsilon$  equal to 0.43 and the refractive index as  $n = 3$ . The calculation is performed from  $kR = 2$  to 25 using the boundary element method (Wiersig, 2003).

The first noticeable feature in the spectrum is that the local maximum of high- $Q$  modes are formed by convex curved series of modes and these convex curved series appear repeatedly in the spectrum (denoted by different symbols in Fig. 7.6). Interestingly, the emission directionality of the high- $Q$  modes display the strongest deviation from the unidirectionality measured by

$$U = \int_0^{2\pi} d\phi f(\phi) \cos \phi, \tag{7.4}$$

where  $f(\phi)$  is the normalized far-field emission distribution of a mode. This observation implies that the chaotic diffusion is suppressed in some way and we assume the effect of partial barrier is the reason.

A convincing clue for this phenomena can be found in configuration distributions of the high- $Q$  modes. Figure 7.7a shows the configurational



7.7 Computed optical mode in a limaçon microcavity: (a) configurational field distribution. The mode has well-defined mode numbers, 1 in radial and 16 in azimuthal degree of freedom. The distribution is fit to the pair of period-4 orbits from the inside. (b) Phase space portrait. From the initial line (dashed lines) the partial barrier (solid line) and turnstile ( $W_4$ ) of period-4 orbit by forward and backward iterations. The Husimi distribution of the mode of (a) is backgrounded. (c) Conjugate point search by ray tracing. Focal points marked by small circles corresponds to the conjugate points.

distribution of a mode around the top of the second mode series in Fig. 7.6a. As a striking feature, this distribution is regular. In general, a mode in a system with underlying chaotic ray dynamics does not have well-defined mode numbers along each degree-of-freedom; however, the mode in Fig. 7.7a shows a reasonably countable number of nodes along the radial and the axial direction. Also an interesting correlation between this regular distribution and a pair of periodic orbits with four bounces is observed. In Fig. 7.7a it can be seen that the internal decay of the mode distribution is well described by a pair of period-4 orbits whose existence is supported by Poincaré–Birkhoff’s theorem (Meiss, 1992). More interestingly, each curved mode series in Fig. 7.6a has a corresponding periodic orbit in increasing order as such confining structure. For instance, all the modes in the first curved series have a pair of period-3 orbit and the third curved series have period-5 orbit, etc.

From these findings, we conjecture that each period orbit plays a role of a partial barrier to form high- $Q$  modes with the following mechanism: when a periodic orbit is able to hold a mode and the action transport of the periodic orbit is less than the resolution of the mode, a WG mode with a high  $Q$ -factor can be constructed by the periodic orbit. However, when the mode becomes able to resolve the action transport, the periodic orbit can not confine a WG mode anymore.

To confirm this hypothesis we quantify the action transport of each periodic orbit. Figure 7.7b shows the phase space section with the Husimi distribution of the mode (Hentschel *et al.*, 2003; Tureci *et al.*, 2005), representing the wave analogue of the Poincaré SOS, in Fig. 7.7a. This smoothing of the Wigner function displays the ray content of the field at the cavity boundary.

The Husimi distribution is located above the fixed points of the pair of period-4 orbits, which are denoted by crosses and circles. To quantify the action transport, we set the initial conditions on the line connecting two consecutive fixed points (crosses) through another fixed point (circle), as given by the dashed line in Fig. 7.7b. Then this initial line is backward and forward iterated until it reaches the central gap marked by a triangle pointing upwards in Fig. 7.7b. By the resulting images of the iteration, two areas are enclosed at the central gap. The action transport of the period-4 orbits can be defined by these two areas that are called ‘turnstile’ (Meiss, 1992) and marked by  $W_4$  in Fig. 7.7b.

By the whole images of the iteration (solid lines in Fig. 7.7b), the partial barrier of period-4 orbit can be defined and the phase space is divided into two parts, the upper and the lower with respect to the partial barrier. According to the Husimi distribution, the mode is located in the upper part and we denote its area  $A_4$ .

Using the two entities around the partial barrier, we set the entering condition that indicates when a mode becomes confined by a periodic orbit and the escaping condition indicating when the confinement of the periodic orbit is resolved.

First, we derive the entering condition using the analogy of the regular mode configuration to a circular microcavity. Due to the integrability of the circular microcavity, the analytic criterion for a mode confined by a periodic orbit is available (Brack and Bhaduri, 2008). We modify this criterion in terms of the area above the partial barrier,  $A_p$  for a  $p$ -periodic orbit:

$$\operatorname{Re}(nkR) > \frac{(\pi/4) + \alpha_p}{\sqrt{1 - (A_p/S)^2} - (A_p/S) \cos^{-1}(A_p/S)}, \quad [7.5]$$

where  $S$  is the total area of the phase space and  $\alpha_p$  is the phase shift from the reflection on the cavity boundary.

Second, the area of the turnstile,  $W_4$  is semiclassically quantized to find the minimum wave number to resolve this area in phase space. In addition, we have to consider conjugate points to take into account of the additional phase sliding (Creagh *et al.*, 1990). The number of the conjugate points can be certified by focuses from a ray-tracing simulation with a small bundle of rays around periodic orbits, and each conjugate point is associated with a  $\pi/2$ -phase sliding. In Fig. 7.7c, we notice that two period-4 orbits have different numbers of conjugate points, that is, the diamond shaped orbit has three conjugate points while the square shaped orbit has four points on it. Characteristically, the limaçon cavity shows the difference of one in the number of conjugate points on each pair of periodic orbits. By taking all the

above factors into account the general escaping condition for a  $p$ -periodic orbit can be derived as follows:

$$\operatorname{Re}(nkR) \leq \frac{\pi}{2W_p}. \quad [7.6]$$

In the derivation of this inequality, it is not needed to explicitly consider the Goos–Hänchen effect, because the total phase slidings of the pair of  $p$ -periodic orbit reflection are almost same, that is, the phase differences are negligible. This can be seen from the positions of the fixed points in the phase space in Fig. 7.7b.

The obtained entering and escaping conditions for each periodic orbit are compared to the spectrum. In Fig. 7.6a we denote the entering conditions by  $N_p$  and the escaping conditions by  $E_p$  for each  $p$ -periodic orbit. The conditions indicate the point of appearance and disappearance of each curved series of modes very consistently.

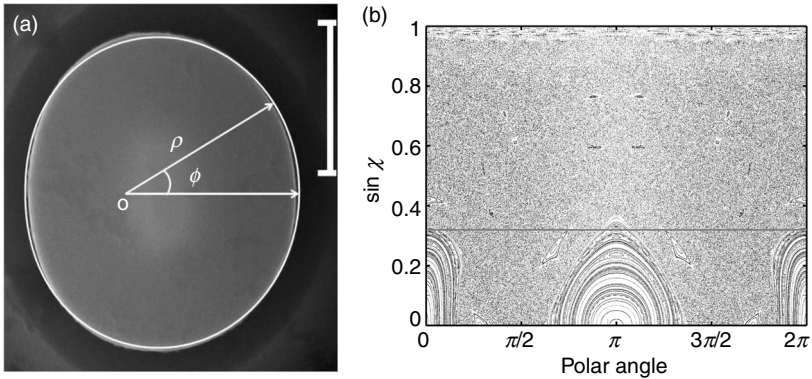
By the suppression of chaotic diffusion, the worse directional emission from the high- $Q$  modes can also be understood. When the chaotic diffusion is hindered by partial barriers, the only available channel to emit radiation is evanescent leakage, which leads to bidirectional emission tangential to the cavity boundary. This results in the reduction of the directionality measure.

## 7.4 Wavelength-scale asymmetric resonant microcavity lasers

With the help of the formation of high- $Q$  modes due to partial barriers and the extended ray dynamics, our goal in the present set of experiments is to exploit new behaviors that might occur in wavelength scale ARC microcavity lasers, and specifically in the limaçon microcavity.

We fabricated GaAs microdisk lasers with embedded InAs QDs as the gain media. The sample is grown on GaAs substrate by molecular beam epitaxy. The layer structure consists of 1000 nm  $\text{Al}_{0.68}\text{Ga}_{0.32}\text{As}$  and 265 nm GaAs. Inside the GaAs layer there are three monolayers of InAs QDs equally spaced by 25 nm GaAs barriers. Standard photolithography is used to define a limaçon shaped microdisk with  $R = 3.75 \mu\text{m}$  and  $\varepsilon = 0.43$ . Next GaAs and AlGaAs are etched nonselectively in a mixture of  $\text{HBr}:\text{H}_2\text{O}_2:\text{H}_2\text{O}$  with the ratio 4:1:25. The etching is nearly isotropic, and decreasing the radius of microdisk by controlling the etching time (Song *et al.*, 2009a). Finally 2.5% diluted HF is used to etch the AlGaAs and form a pedestal underneath the GaAs disk (Song *et al.*, 2009a). Figure 7.8a is a top-view scanning electron microscope (SEM) image of the fabricated disk. Its shape is fitted by

$$\rho(\phi) = R(1 + \varepsilon \cos \phi)(1 - \varepsilon_1 \cos 2\phi) + d, \quad [7.7]$$

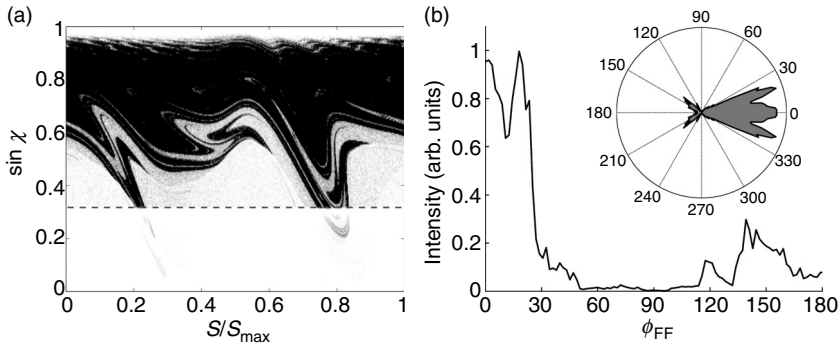


7.8 (a) The top-view SEM image of a GaAs disk. The scale bar is 1  $\mu\text{m}$ . The cavity shape is defined in polar coordinates as in Equation [7.7]. (b) Conventional ray tracing result with closed cavity boundary. The ray dynamics is predominantly chaotic with two regular regions below the critical line  $\sin \chi_c = 1/n$ .

where  $R = 890 \text{ nm}$ ,  $\varepsilon = 0.28$ ,  $\varepsilon_1 = 0.06$  and  $d = 60 \text{ nm}$ . This radius is much smaller than all the previous reports (Shinohara *et al.*, 2009; Song *et al.*, 2009b; Yan *et al.*, 2009; Yi *et al.*, 2009). As shown in Fig. 7.8a, the angle  $\phi$  uniquely specifies a point on the boundary, but to avoid confusion, below we use  $\phi_{\text{FF}}$  to designate far-field directions, and the arclength  $S$ , measured from the boundary point on the positive  $x$ -axis and normalized to the perimeter, to specify points on the boundary.

Although the fabricated cavity shape slightly deviates from the limaçon, the ray dynamics is very similar. Figure 7.8b shows the result of ray tracing in the closed cavity (with perfect reflection of light from the boundary). Similar to the case of the limaçon cavity, the ray dynamics is predominantly chaotic. Without escape from the boundary, a typical trajectory could explore almost the entire phase space in a random-looking fashion. In addition to the chaotic orbits, there are stable periodic orbits that correspond to a few tiny islands and two big islands near  $\sin \chi = 0$ . Unstable periodic orbits also exist among the chaotic sea. WG trajectories are confined in the narrow bands  $|\sin \chi| > 0.99$ .

Next we performed the (conventional) ray-tracing simulation in an open cavity from which light can escape via refraction at the boundary. From the lowest order TE waveguide mode in the GaAs layer, we computed the effective index of refraction  $n_e = 3.13$ . The initial rays with identical amplitudes are uniformly distributed in the phase space above the critical line. At each reflection from the boundary, the amplitude of a ray is reduced according to the Fresnel law. Tracing of one ray is stopped after its amplitude falls below a certain value. Figure 7.9a shows the sum of intensities of all iterations by



7.9 (a) Conventional ray tracing simulation in the dielectric disk of a refractive index 3.13 with boundary given by Equation [7.7] showing the rays escape along the unstable manifold in the leaky area. (b) Far-field emission pattern predicted by the ray tracing simulation. The inset is the corresponding angular distribution of far-field intensity.

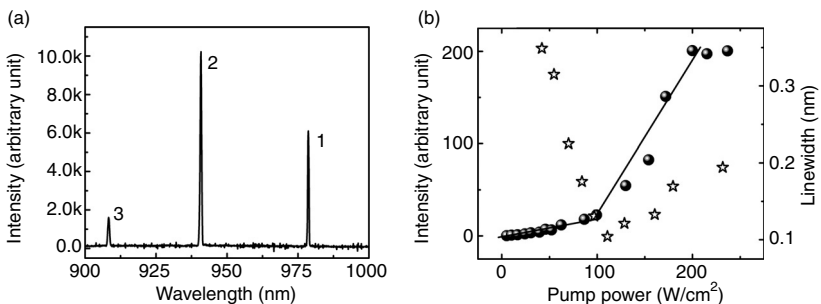
tracing 20 000 rays propagating CCW inside the cavity. It reveals that the rays diffuse along the unstable manifolds toward the leaky region of  $\chi < \chi_c = \arcsin(1/n_e)$ , where  $\chi_c$  is the critical angle for total internal reflection. The inset of Fig. 7.9b is an angular plot of the far-field emission intensity. The directed flow of rays in the phase space produces an output beam in the direction  $\phi_{\text{FF}} = 0^\circ$ .

We have seen that chaotic ray dynamics in the semiclassical region of large  $kR$  (small wavelength) can lead to highly directional emission. It is natural and interesting to ask whether such directional outputs can be realized in small cavities such as wavelength scale or subwavelength scale, where the  $kR$  is close to 1. In Section 7.3.2 it was demonstrated that in this regime WG modes with high-quality factor can still exist due to partial barriers in phase space. However, the emission is dominated by tunneling and therefore less directional. The lower- $Q$  modes with small angular momentum below partial barriers will have more anisotropic emission, but these modes would not show up in the lasing spectrum because their lasing thresholds are too high.

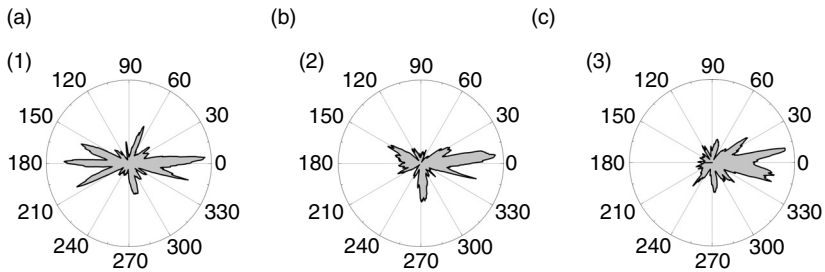
Let us see what happens experimentally. In our lasing experiment, the sample is mounted in a liquid Helium cryostat with the substrate temperature kept at 10 K and optically pumped by a mode-locked Ti: Sapphire laser (pulse width 200 fs, 76 MHz repetition rate). The pump wavelength is 790 nm. A long working distance is used to focus pump beam normally to the microdisk from the top and collect the emitted laser emission reversely. Time-integrated spectra are taken by a spectrometer with a cooled charge-coupled device (CCD) array detector. Because we measure the lasing spectrum, only the high- $Q$  modes of frequencies within the gain spectrum are

accessible. The gain spectrum of InAs QDs is inhomogeneously broadened and has a large width of about 80 nm, allowing us to observe several lasing modes in the small disk despite the large mode spacing. The laser emission spectrum depicted in Fig. 7.10a consists of three peaks at vacuum wavelengths  $\lambda = 908, 942$  and  $978$  nm. Figure 7.10b shows the dependence of emission intensity on the pump intensity. When the pump intensity is higher than  $\approx 100$  W/cm<sup>2</sup>, the output intensity increases dramatically, indicating a threshold behavior at  $\approx 100$  W/cm<sup>2</sup>. We also measured the linewidth of the mode at 908 nm as a function of pump intensity. It decreases first to 0.1 nm, and then increases, mostly due to temporal shift of lasing frequency (Pompe *et al.*, 1995). In our time-integrated measurement of lasing spectrum, the transient frequency shift results in a broadening of the lasing line. Such broadening increases with the hot carrier density and becomes dominant at higher pump.

To measure the far-field pattern of laser emission from a deformed micro-disk cavity, we fabricated a large ring structure around each microdisk. The in-plane laser emission from the disk edge propagates to the ring and is scattered out of the plane. The scattered light pattern is imaged by the objective lens to a CCD camera. Since the ring radius exceeds  $4R^2/\lambda$ , the scattered light intensity along the ring reflects the far-field emission pattern of the microdisk. Bandpass filters have been placed in front of the CCD camera to measure the far-field patterns of these three modes. The measured far-field patterns are shown in Fig. 7.11. All the three lasing modes (labeled 1–3) have significantly different far-field patterns. Mode 3 has output predominantly in the forward direction ( $\phi_{\text{FF}} = 0^\circ$ ), while mode 1 displays bidirectional emission in both forward and backward ( $\phi_{\text{FF}} = 180^\circ$ ) directions. Mode



7.10 (a) Measured laser emission spectrum at the incident pump intensity of  $191$  W/cm<sup>2</sup>. (b) The measured emission intensity (dots) and linewidth (stars) of the peak 3 as a function of pump intensity. A clear threshold behavior can be observed at around  $100$  W/cm<sup>2</sup>. The linewidth decreases first and increases at higher power because of the hot carrier effect caused by ultrashort laser pulse.

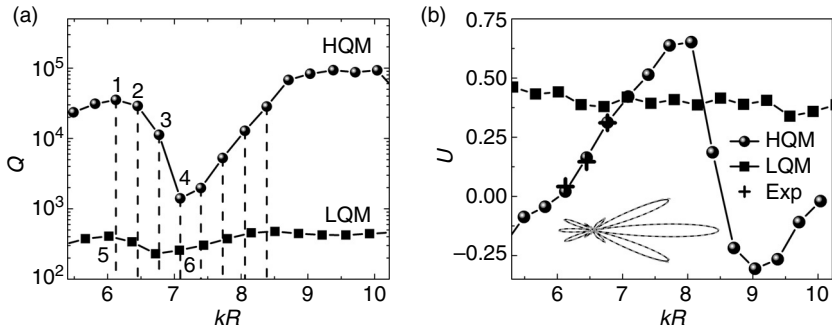


7.11 (a)–(c) Measured far-field patterns for the lasing modes 1, 2 and 3 in Fig. 7.10a. The incident pump intensity is kept at  $191 \text{ W/cm}^2$ . (Source: Reprinted from Song *et al.* (2010) with kind permission from *Physical Review Letters*.)

2 is the intermediate between 1 and 3. This phenomenon is distinct from that of larger limaçon cavities that have nearly identical unidirectional emission patterns for all lasing modes. It indicates the breakdown of ray dynamics in the wavelength scale cavities. The failure of the (conventional) ray model in wavelength-scale deformed microdisk lasers is expected; this statistical model is more appropriate for multimode lasing in the limit of short wavelength  $kR \gg 1$ ,  $k = 2\pi/\lambda$ . However, the persistence of unidirectional emission to such small scales (mode 3) is surprising.

To explain this interesting finding we solved the electromagnetic wave equations for the cavity resonances after extracting the actual disk shape and dimension from the SEM images. Three numerical methods were used: a finite-difference time-domain (FDTD) algorithm (Song *et al.*, 2009b), the scattering matrix approach (Tureci *et al.*, 2005) and boundary element method (Wiersig, 2003) and they give consistent results. We find a set of high- $Q$  modes (HQM) with constant frequency spacing and similar spatial profile; in most cases these modes look like WG modes, with vanishing intensity towards the disk center. However, as shown in Fig. 7.12a, their  $Q$  values have an unusual non-monotonic variation with frequency, exhibiting a minimum at  $kR \approx 7.1$ . In addition we observe a low- $Q$  mode (LQM) series in the same frequency range, the relevance of which will be discussed below. Note that the LQM has lower angular momentum and is therefore localized below the relevant partial barriers. It is therefore not confined by these partial barriers, which leads to a lower  $Q$ . For the same reason it can follow the unstable manifold, which should result in unidirectional emission.

To characterize the directionality of the output we use the measure in Equation [7.4];  $U = 0$  corresponds to isotropic or bidirectional emission, whereas positive (negative)  $U$  corresponds to emission primarily towards  $\phi_{\text{FF}} = 0^\circ (180^\circ)$ . We find that as the normalized frequency  $kR$  decreases from 10 to 5.5, the value of  $U$  first increases from approximately 0 to 0.6 and then

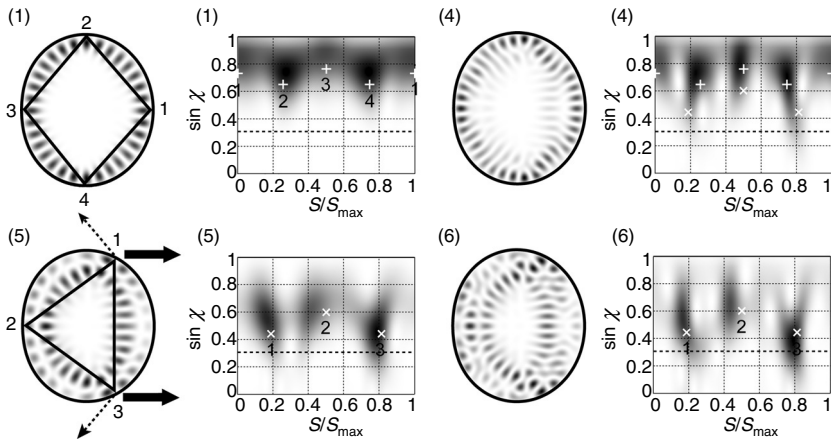


7.12 (a) Calculated  $Q$  values for the high-quality modes (HQMs, dots) and the low-quality modes (LQMs, squares). Modes marked 1, 2 and 3 correspond to the three lasing modes in Fig. 7.10a. (b) Directionality  $U$  of the HQMs and LQMs versus  $kR$ . Crosses are  $U$  values of the three lasing modes in Fig. 7.10a. Inset: calculated far-field patterns for modes labeled 4 (solid line) and 6 (dashed line) in (a). (Source: Reprinted from Song *et al.* (2010) with kind permission from *Physical Review Letters*.)

decreases to 0. The calculated far-field patterns confirm a transition from bidirectional emission to unidirectional emission, and back to bidirectional emission. The frequency of maximum  $U$  is close to but not equal to that of the mode with the minimum  $Q$  for the high- $Q$  mode series. Our lasing experiment, however, cannot detect the lowest  $Q$  mode of the series (labeled 4 in Fig. 7.12) because it does not lase, instead the three modes it measures (Fig. 7.10a) are the ones on the low  $kR$  (long wavelength) side of the  $Q$  dip and labeled 1, 2 and 3 in Fig. 7.12a. The calculated angular distributions of far-field intensities of modes 1–3 resemble the measured ones, which change from bidirectional output to unidirectional emission. The values of  $U$  computed from the measured far-field patterns of three lasing modes are also plotted in Fig. 7.12b as crosses. They are in good agreement with the values calculated from the wave simulations.

The dip in  $Q$  of the high- $Q$  mode series is associated with the unidirectional emission; we therefore analyze the highest and lowest  $Q$  modes (1 and 4 in Fig. 7.12a) on the long wavelength side for a clue to the mechanism of the unidirectional emission. The intensity plots for these two modes in the upper panels of Fig. 7.13 show that while mode 1 is a smooth deformation of a WG mode with angular momentum mode number  $m = 16$ , mode 4 appears to be a superposition of a similar WG mode and a much lower angular momentum mode with significant intensity away from the boundary.

The effect of this superposition in mode 4 is most clearly seen by taking the field distribution ('photon wavefunction') and performing the Husimi projection onto the SOS. For mode 1 the Husimi function has four maxima



7.13 Calculated spatial distribution of electric field intensity and Husimi function of the cavity modes labeled 1, 4, 5 and 6 in Fig. 7.12a. (Source: Reprinted from Song *et al.* (2010) with kind permission from *Physical Review Letters*.)

at specific locations on the boundary and specific ray angles of incidence corresponding to the ‘diamond orbit’ that is superposed on the wavefunction in Fig. 7.13. The Husimi function below the critical angle has the largest amplitude near the bounce points labeled 2, 4, which are the highest curvature of the four bounce points and most of the emission occurs near there ( $\phi_{\text{FF}} = 0^\circ$  and  $180^\circ$ ). Note that the SOS for this mode (Fig. 7.13) has approximate symmetry around the points  $s = 0, 0.5$ . Such a Husimi function must lead to approximately equal emission into the forward and backward quadrants as we find for this mode. The small residual symmetry breaking arises from the relatively small distortion of the diamond orbit from reflection symmetry around the vertical axis of the limaçon. In contrast, the Husimi function for mode 4 (Fig. 7.13) shows a large symmetry breaking around  $s = 0.5$ , which results in unidirectional emission primarily from region around  $s = 0.8$  on the boundary in the  $\phi_{\text{FF}} = 0^\circ$  direction. This is in agreement with the unstable manifold in Fig. 7.9a. Note that only the upper half ( $\sin \chi > 0$ ) portion of the SOS is displayed; it corresponds to CCW circulating rays. The Husimi function in the lower half is reflected around  $s = 0.5$  and indicates strong emission from  $s = 0.2$  but of the oppositely circulating ray, leading to far-field emission in the  $\phi_{\text{FF}} = 0^\circ$  direction as well.

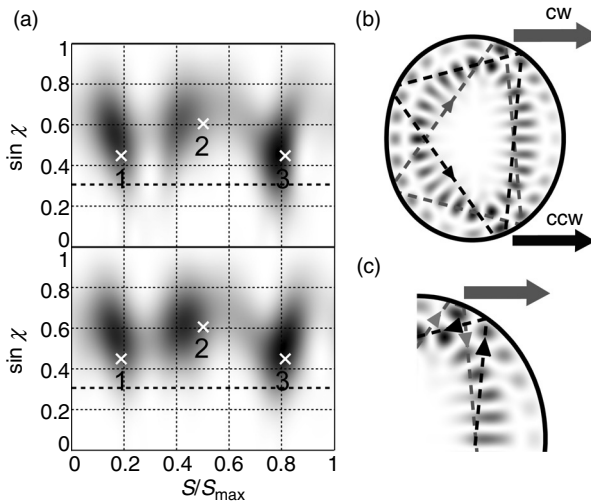
It is not easy to tell from the Husimi functions why mode 4 is much leakier than mode 1; however, this becomes evident from considering modes 5 and 6 of the LQM series also shown in Fig. 7.12a. This mode series has Husimi functions well localized on a three-bounce periodic orbit drawn on the spatial intensity distribution of mode 5 in Fig. 7.13. Since this orbit has

two bounce points (labeled 1 and 3) much closer to the critical angle, this mode series is much lower  $Q$  than the series based on the diamond orbit, and does not lase experimentally. This is consistent with our expectation that the more directional modes would not appear in the lasing spectrum.

The two series of HQMs and LQMs have different frequency spacing and thus it is possible to have particular pairs of modes (one from each series) that are nearly degenerate in their frequencies. This is exactly what happens for the modes labeled 4 and 6 in Fig. 7.12a. In general, as two resonances approach each other, they may couple either strongly or weakly. In the case of weak coupling, the frequencies of two modes cross and their  $Q$  values anti-cross. There is no ‘exchange of identity’. For strong coupling, the frequencies anti-cross and the  $Q$ s cross; there is an ‘exchange of identity’ (Wiersig, 2006; Wiersig and Hentschel, 2006; Unterhinninghofen *et al.*, 2008; Lee *et al.*, 2009a, 2009b; Song and Cao, 2010). The HQM and LQM are weakly coupled, as their frequencies cross and  $Q$ s anti-cross in Fig. 7.12a. The spatial intensity plots in Fig. 7.13 reveals that mode 4 is a mixture of modes 1 and 5; this is clear for mode 6 as well, which has ‘more’ of the leakier mode 5 and hence lower  $Q$ . Moreover, the phase space structure of modes 4 and 6 (Husimi functions in Fig. 7.13) are almost the same near and below the critical line. Consequently, their far-field emission patterns are nearly identical as can be seen in the inset of Fig. 7.12b. These data confirm that they are coupled and the output is dominated by the LQM component. Thus the violation of our expectation that HQMs would be approximately isotropic emitters arises from the weak coupling of a high- $Q$  mode to a directional LQM, which does not strongly degrade the  $Q$  but enables substantially directional output. While mode 4 is the most hybridized (and therefore too low  $Q$  to lase), the mode coupling for the experimentally observed mode 3 is sufficient to obtain directional emission. Its  $Q$  exceeds 10 000, high enough to lase with modest pumping.

We make two notes here: (i) the coupling discussed above is the linear coupling of two eigenvalues near a frequency crossing, not the non-linear coupling of modes due to spectral hole-burning, which is negligible in our device due to the inhomogeneous gain broadening; (ii) previously Wiersig and Hentschel (2006) proposed exactly this mechanism for obtaining the high- $Q$  mode with directional emission in a circular dielectric disk with an air hole. However, the existence of nearly degenerate modes with different far-field patterns in general smears out the output directionality. Such a problem does not exist in our case.

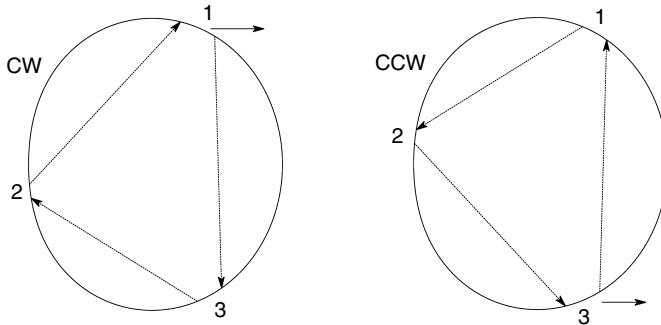
A final intriguing question is how to explain the broken symmetry of emission of the LQM series based on the triangle orbit. The orbit itself has symmetric bounce points (labeled 1 and 3 in the spatial intensity plot of mode 5 in Fig. 7.13) that are at lower incidence angle than bounce 2. Hence most of the emission occurs at bounces 1 and 3. A ray can traverse



7.14 (a) Husimi functions of incident (top) and emergent (bottom) waves for mode 5. (b,c) CW and CCW pseudo-orbits extracted from the actual bouncing points in the Husimi distributions in (a).

the triangle either CW or CCW, and by symmetry should emit at each point into the forward *and* backwards directions. If this symmetry were obeyed by the photon wavefunction the unidirectionality would be lost; but the Husimi function of mode 5 in Fig. 7.13 describing CCW rays ( $\sin \chi > 0$ ) violates this symmetry and is indeed leakier at point 3 than point 1. The Husimi function for CW rays ( $\sin \chi > 0$ ) has the opposite asymmetry and is leakier at point 1, leading to the unidirectional emission.

This symmetry breaking can only come from the openness of the system, which distinguishes incident and reflected (emergent) rays. A qualitative explanation for it can be given by the two wave effects, GHS and FF, as discussed in Section 7.3.1. As was pointed out by Altmann *et al.* (2008), the extended ray dynamics including GHS and FF violates the chiral symmetry of the periodic orbits; a periodic orbit such as the triangle will now break into two distinct CW and CCW periodic pseudo-orbits. To confirm these two effects, we have analyzed the incident and emergent Husimi distributions of mode 5 (Fig. 7.14a). The crosses represent the bouncing points of the original symmetric triangle orbit. It is evident from Fig. 7.14a that the Husimi intensity maxima deviate from the ray prediction. The lateral and vertical shifts between the maxima of incident and emergent Husimis at the same bouncing point originates from the GHS and the FF (Unterhinninghofen and Wiersig, 2000; Schomerus and Hentschel, 2006). By extracting the location of each bouncing point from the intensity maxima in the Husimi distributions, we plot in Fig. 7.14b the CW and CCW pseudo-orbits that compose



7.15 Expected light emission pattern from CW and CCW rays for the asymmetric period-3 orbits of the extended ray dynamics. Both CW and CCW rays emit in the forward direction.

mode 5. The CW orbit has a smaller angle of incidence at bounce 1 than does the CCW orbit, leading to unidirectional forward emission dominated by the CW beam (Fig. 7.14c). The corresponding effect occurs for the CCW orbit near bounce point 3, so it dominates the emission, again in forward direction.

The conclusions drawn from Fig. 7.14 are confirmed independently by direct calculations based on the extended ray dynamics including the GHS and the FF effect as described in Section 7.3.1. Figure 7.15 shows the period-3 orbits corresponding to the mode in Fig. 7.14b. In the case of CW (CCW) motion the angle of incidence is smallest at point 1 (3) giving rise to the strongest emission there. In both cases the emission goes in the same direction leading to the unidirectional light emission.

## 7.5 Conclusions

The highly directional output from a wavelength-scale GaAs microdisk laser with embedded InAs quantum dots is demonstrated. The radius of the deformed microdisk is comparable to the emission wavelength. The unidirectional light emission is traced back to the weak coupling of isotropic HQM to directional LQMs and chiral symmetry breaking of waves. The latter is described by an extended ray dynamics that includes the Goos–Hänchen shift and the Fresnel filtering. The existence of HQM in such a strongly deformed geometry is explained in terms of partial barriers in phase space of rays that turn into complete barriers for waves in wavelength-scale microcavities. Further numerical simulations indicate that similar behavior occurs for a wide range of cavity deformations around that studied here and indices of refraction, making our design potentially useful for GaN lasers at blue and near-ultraviolet wavelengths as well.

The wavelength-scale microdisks discussed in this chapter have a high potential to be used in nanophotonic circuits, on-chip optical interconnects, nanoplasmonics, and very local chemical and biological sensing. However, there are still several new challenges ahead. Although the obtained quality factors from our deformed microdisks are sufficiently high to achieve lasing operation, they are too low for applications in cavity quantum electrodynamics. It is therefore interesting to find new ways to get deformed wavelength-scale microdisks with higher quality factors while maintaining their original unidirectional outputs. Another technical challenge is to push the size of such deformed microdisks to the subwavelength scale. This further reduction of laser size provides an opportunity to exploit novel functionalities that cannot be realized in larger devices.

## 7.6 Acknowledgment

Financial support from the DFG research group 760, NIST under Grant No. 70NANB6H6162, and NSF under Grants No. DMR-0808937 and No. DMR-0908437 is acknowledged.

## 7.7 References

- Altmann, E. G., G. Del Magno, and M. Hentschel. Non-Hamiltonian dynamics in optical microcavities resulting from wave-inspired corrections to geometric optics. *Euro. Phys. Lett.*, **84**:10008, 2008.
- Artmann, K. Berechnung der Seitenversetzung des totalreflektierten Strahles. *Ann. Phys. (Leipzig)*, 437:87–102, 1948.
- Berry, M. V. Regularity and chaos in classical mechanics, illustrated by three deformations of a circular ‘billiard’. *Eur. J. Phys.*, **2**:91–102, 1981.
- Birkhoff, G. D. Proof of Poincaré’s geometric theorem. *Trans. Am. Math. Soc.*, **14**:14–22, 1913.
- Brack, M. and R. K. Bhaduri. *Semiclassical Physics*. Westview Press, Boulder, 2008.
- Chern, G. D., H. E. Tureci, A. D. Stone, R. K. Chang, M. Kneissl, and N. M. Johnson. Unidirectional lasing InGaN multiple-quantum-well spiral-shaped micropillars. *Appl. Phys. Lett.*, **83**:1710–1712, 2003.
- Creagh, S. C., J. M. Robbins, and R. G. Littlejohn. Geometrical properties of Maslov indices in the semiclassical trace formula for the density of states. *Phys. Rev. A*, **42**:1907–1922, 1990.
- Gao, J., P. Heider, C. J. Chen, X. Yang, C. A. Husko, and C. W. Wong. Observations of interior whispering-gallery modes in asymmetric optical resonators with rational caustics. *Appl. Phys. Lett.*, **91**:181101, 2007.
- Gmachl, C., F. Capasso, E. E. Narimanov, J. U. Nöckel, A. D. Stone, J. Faist, D. L. Sivco, and A. Y. Cho. High-power directional emission from microlasers with chaotic resonators. *Science*, **280**:1556–1564, 1998.
- Goos, F. and H. Hänchen. Ein neuer und fundamentaler Versuch zur Totalreflexion. *Ann. Phys. (Leipzig)*, **436**:333, 1947.

- Heller, E. J. Bound-states eigenfunctions of classically chaotic Hamiltonian systems: Scars of periodic orbits. *Phys. Rev. Lett.*, **53**:1515–1518, 1984.
- Hentschel, M., H. Schomerus, and R. Schubert. Husimi functions at dielectric interfaces: Inside-outside duality for optical systems and beyond. *Europhys. Lett.*, **62**:636–642, 2003.
- Jackson, J. D. *Classical Electrodynamics*. John Wiley and Sons, New York, 1962.
- Lai, H. M., F. C. Cheng, and W. K. Tang. Goos-Hänchen effect around and off the critical angle. *J. Opt. Soc. Am. A*, **3**:550, 1986.
- Lebental, M., J. S. Lauret, R. Hierle, and J. Zyss. Highly-directional stadium-shaped polymer microlasers. *Appl. Phys. Lett.*, **88**:031108, 2006.
- Lebental, M., J. S. Lauret, J. Zyss, C. Schmit, and E. Bogomolny. Directional emission of stadium-shaped microlasers. *Phys. Rev. A*, **75**:033806, 2007.
- Lee, S.-B., J. Yang, S. Moon, S.-Y. Lee, J.-B. Shim, S. W. Kim, J.-H. Lee, and K. An. Quasieigenstate evolution in open chaotic billiards. *Phys. Rev. A*, **80**:011802, 2009a.
- Lee, S.-B., J. Yang, S. Moon, S.-Y. Lee, J.-B. Shim, S. W. Kim, J.-H. Lee, and K. An. Observation of an exceptional point in a chaotic optical microcavity. *Phys. Rev. Lett.*, **103**:134101, 2009b.
- Lichtenberg, A. J. and M. A. Lieberman. *Regular and Chaotic Dynamics*. Springer, Berlin, 1992.
- Meiss, J. D. Symplectic maps, variational principles and transport. *Rev. Mod. Phys.*, **64**:795–848, 1992.
- Nöckel, J. U. *Resonances in Nonintegrable Open Systems*. PhD thesis, Yale University, 1997.
- Nöckel, J. U. and A. D. Stone. Chaos in optical cavities. *Nature (London)*, **385**:45–47, 1997.
- Nöckel, J. U., A. D. Stone, and R. K. Chang.  $Q$  spoiling and directionality in deformed ring cavities. *Opt. Lett.*, **19**:1693–1695, 1994.
- Nöckel, J. U., A. D. Stone, G. Chen, H. L. Grossman, and R. K. Chang. Directional emission from asymmetric resonant cavities. *Opt. Lett.*, **21**:1609–1611, 1996.
- Pompe, G., T. Rappen, M. Wehner, F. Knop, and M. Wegener. Transient-response of a short-cavity semiconductor-laser. *Phys. Stat. Sol. B*, **188**:175–180, 1995.
- Lord Rayleigh. *The Theory of Sound*. American edition, Dover, New York, 1945. First published 1877.
- Schomerus, H. and M. Hentschel. Correcting ray optics at curved dielectric microresonator interfaces: Phase-space unification of Fresnel filtering and the Goos-Hänchen shift. *Phys. Rev. Lett.*, **96**:243903, 2006.
- Schwefel, H. G. L., N. B. Rex, H. E. Tureci, R. K. Chang, A. D. Stone, T. Ben-Messaoud, and J. Zyss. Dramatic shape sensitivity of directional emission patterns from similarly deformed cylindrical polymer lasers. *J. Opt. Soc. Am. B*, **21**:923–934, 2004.
- Shim, J.-B., S.-B. Lee, S. W. Kim, S.-Y. Lee, J. Yang, S. Moon, J.-H. Lee, and K. An. Uncertainty-limited turnstile transport in deformed microcavities. *Phys. Rev. Lett.*, **100**:174102, 2008.
- Shinohara, S., M. Hentschel, J. Wiersig, T. Sasaki, and T. Harayama. Ray-wave correspondence in limaçon-shaped semiconductor microcavities. *Phys. Rev. A*, **80**:031801(R), 2009.
- Song, Q. H. and H. Cao. Improving optical confinement in nanostructures via external mode coupling. *Phys. Rev. Lett.*, **105**:053902, 2010.
- Song, Q. H., H. Cao, S. T. Ho, and G. S. Solomon. Near IR subwavelength microdisk lasers. *Appl. Phys. Lett.*, **94**:061109, 2009a.

- Song, Q. H., W. Fang, B. Liu, S. T. Ho, G. S. Solomon, and H. Cao. Chaotic microcavity laser with low threshold and unidirectional output. *Phys. Rev. A*, **80**:041807(R), 2009b.
- Song, Q. H., L. Ge, A. D. Stone, H. Cao, J. Wiersig, J.-B. Shim, J. Unterhinninghofen, W. Fang, and G. S. Solomon. Directional laser emission from a wavelength-scale chaotic microcavity. *Phys. Rev. Lett.*, **105**:103902, 2010.
- Stöckmann, H.-J. *Quantum Chaos*. Cambridge University Press, Cambridge, UK, 2000.
- Tanaka, T., M. Hentschel, T. Fukushima, and T. Harayama. Classical phase space revealed by coherent light. *Phys. Rev. Lett.*, **98**:033902, 2007.
- Tureci, H. E. and A. D. Stone. Deviation from Snell's law for beams transmitted near the critical angle: Application to microcavity lasers. *Opt. Lett.*, **27**:7–9, 2002.
- Tureci, H. E., H. G. L. Schwefel, Ph. Jacquoud, and A. D. Stone. Modes of wave-chaotic dielectric resonators. *Prog. Opt.*, **47**:75–137, 2005.
- Unterhinninghofen, J. and J. Wiersig. Interplay of Goos-Hänchen shift and boundary curvature in deformed microdisks. *Phys. Rev. E*, **82**:026202, 2010.
- Unterhinninghofen, J., J. Wiersig, and M. Hentschel. Goos-Hänchen shift and localization of optical modes in deformed microcavities. *Phys. Rev. E*, **78**:016201, 2008.
- Unterhinninghofen, J., U. Kuhl, J. Wiersig, H.-J. Stöckmann, and M. Hentschel. Measurement of the Goos-Hänchen shift in a microwave cavity. *New J. Phys.*, **13**:023013, 2011.
- Wiersig, J. Boundary element method for resonances in dielectric microcavities. *J. Opt. A: Pure Appl. Opt.*, **5**:53–60, 2003.
- Wiersig, J. Formation of long-lived, scar-like modes near avoided resonance crossings in optical microcavities. *Phys. Rev. Lett.*, **97**:253901, 2006.
- Wiersig, J. and M. Hentschel. Unidirectional light emission from high- $Q$  modes in optical microcavities. *Phys. Rev. A*, **73**:031802(R), 2006.
- Wiersig, J. and M. Hentschel. Combining directional light output and ultralow loss in deformed microdisks. *Phys. Rev. Lett.*, **100**:033901, 2008.
- Yan, C., Q. J. Wang, L. Diehl, M. Hentschel, J. Wiersig, N. Yu, Pfügel, F. Capasso, M. A. Belkin, T. Edamura, M. Yamanishi, and H. Kan. Directional light emission from microcavity quantum cascade lasers with limaçon-shaped resonator. *Appl. Phys. Lett.*, **94**:251101, 2009.
- Yi, C.-H., M.-W. Kim, and C.-M. Kim. Lasing characteristics of a limaçon-shaped microcavity laser. *Appl. Phys. Lett.*, **95**:141107, 2009.